

Optical EVPA rotations in blazars: testing a stochastic variability model with RoboPol data

S. Kiehlmann,^{1,2,3*} D. Blinov,^{4,5} T.J. Pearson,³ I. Liodakis^{4,6,7}

¹*Aalto University Metsähovi Radio Observatory, Metsähovintie 114, 02540 Kylmälä, Finland*

²*Aalto University Department of Radio Science and Engineering, PL 13000, 00076 Aalto, Finland*

³*Owens Valley Radio Observatory, California Institute of Technology, Pasadena, CA 91125, USA*

⁴*Department of Physics and Institute for Theoretical and Computational Physics, University of Crete, 71003, Heraklion, Greece*

⁵*Astronomical Institute, St. Petersburg State University, Universitetsky pr. 28, Petrodvoretz, 198504 St. Petersburg, Russia*

⁶*Foundation for Research and Technology - Hellas, IESL, Voutes, GR-71110 Heraklion, Greece*

⁷*KIPAC, Stanford University, 452 Lomita Mall, Stanford, CA 94305, USA*

Accepted 2017 August 17. Received 2017 August 16; in original form 2017 June 8.

ABSTRACT

We identify rotations of the polarization angle in a sample of blazars observed for three seasons with the RoboPol instrument. A simplistic stochastic variability model is tested against this sample of rotation events. The model is capable of producing samples of rotations with parameters similar to the observed ones, but fails to reproduce the polarization fraction at the same time. Even though we can neither accept nor conclusively reject the model, we point out various aspects of the observations that are fully consistent with a random walk process.

Key words: polarization – galaxies: active – galaxies: jets – galaxies: nuclei.

1 INTRODUCTION

The variability of the optical polarization fraction and electric vector position angle (EVPA) in blazars has been known since the earliest observations (Kinman 1967). Large, continuous rotations of the EVPA have been reported in various objects, e.g., OJ 287 (Kikuchi et al. 1988), BL Lac (Marscher et al. 2008), PKS 1510–089 (Marscher et al. 2010; Aleksić et al. 2014b), and 3C 279 (e.g. Larionov et al. 2008; Aleksić et al. 2014a; Kiehlmann et al. 2016). Some rotations of the optical EVPA have been reported to be associated with gamma-ray flares (e.g. Marscher et al. 2008; Larionov et al. 2013; Aleksić et al. 2014a), suggesting a potential physical connection between these events.

Various mechanisms have been proposed to explain EVPA rotations. Deterministic models typically assume an ordered magnetic field structure. Examples of such models include the superposition of two or more emission regions (Holmes et al. 1984), a bend of the jet (Nalewajko 2010), and the progression of an emission feature on a helical streamline (Marscher et al. 2008) or a shock (Konigl & Choudhuri 1985; Zhang et al. 2014, 2015) passing through a helical magnetic field. Stochastic models on the other hand assume a tangled magnetic field structure and model a turbulent flow in terms of random cells (e.g. Jones et al. 1985; Marscher 2014;

Kiehlmann et al. 2016). The most recent models of Zhang et al. (2014) and Marscher (2014) focus particularly on the broad-band variability of the polarized and total flux and the potential connection between optical EVPA rotations and high-energy flaring activity.

The RoboPol¹ project, an optical polarization monitoring campaign of an unbiased sample of blazars (Pavlidou et al. 2014), was initiated to study the optical EVPA rotation phenomenon in blazars on a statistical basis and in particular to address the question, whether these rotations are physically connected to the gamma-ray flaring process. Blinov et al. (2015) showed that some but not all rotations in the first season of the RoboPol data could be produced by a random walk process. They also argued that some rotations occur contemporaneously with gamma-ray flares and that the contemporaneity is unlikely to be happening by chance, implying a physical connection between the two events. In comparison, based on a single case study of 3C 279, Kiehlmann et al. (2016) demonstrated that even within the same object some EVPA rotations may be explained by a random walk process, while others cannot. Based on the first and second season data of the RoboPol project, Blinov et al. (2016a) showed that the average polarization fraction during rotations is lower in comparison to non-rotation periods and that it is correlated with the

* E-mail: skiehl@caltech.edu

¹ <http://robopol.org/>

EVPA rotation rate. Additionally, they demonstrated that rotation amplitudes and durations have upper limits. Based on three seasons of data, Blinov et al. (2016b) claim that only a fraction of blazars exhibit large rotations of the EVPA frequently, while others rarely or never show such events. Angelakis et al. (2016) have demonstrated that the EVPA is on average more variable in low synchrotron peaked (LSP) sources than in high synchrotron peaked (HSP) sources.

In this study we use the full data set of three seasons of RoboPol blazar monitoring to test a random walk process scenario. In contrast to the case-by-case study of EVPA rotations in 3C 279 by Kiehlmann et al. (2016) here we follow a statistical approach of testing an entire sample of blazars against a random walk process. With three seasons of data, which have significantly increased the number of observed EVPA rotations, the RoboPol data provide a solid basis for a statistical study. In particular we test whether several of the relations found in Blinov et al. (2016a) and Blinov et al. (2016b) can be explained by a random walk process.

2 DATA AND DATA PROCESSING

The RoboPol main sample is an unbiased, gamma-ray photon-flux-limited sample of 62 gamma-ray-loud blazars, selected from the *Fermi*-LAT Second Source Catalogue (2FGL, Nolan et al. 2012). The sample selection is discussed in detail in Pavlidou et al. (2014) and we follow their source nomenclature. These objects were continuously monitored with the RoboPol polarimeter at the 1.3 meter telescope of the Skinakas observatory for three seasons: May 2013 – November 2013, April 2014 – November 2014, and May 2015 – November 2015. King et al. (2014) describe features of the instrument and the pipeline used for the data reduction. Detailed information on the observations for each season is given in Blinov et al. (2015, 2016a), and Blinov et al. (2016b). Additional quality checks, applied to the data after the automated data reduction, are described in Angelakis et al. (2016).

19 sources in the sample were occasionally observed two to four times during a single night. In 13 of those sources we do not observe significant variability in both the EVPA and at least one Stokes parameter at these time-scales. Here, we average the fractional Stokes parameters $q = QI$, $u = UI$ within time intervals of half a day without removing significant variability. Otherwise some measurements of the rotation variation estimator (explained in Section 3.2) would be strongly affected by extreme rotation rates induced by observational noise on very short time-scales. Six sources with intra-night observations occasionally show significant variability in the EVPA and at least one Stokes parameter: RBPL J1555+1111, RBPL J1653+3945, RBPL J2202+4216, RBPL J2232+1143, RBPL J2243+2021, RBPL J2253+1608. Also for these sources we average fractional Stokes parameters within time intervals of half a day, thus averaging out real intrinsic variability. This is done to avoid complications with the model (Section 4 and following), which cannot cover arbitrarily short time-scales due to its discrete set up of cells and variability. None of the results and conclusions based on the model comparison are affected by the intra-night averaging. A publication that addresses how the identification

Table 1. How many objects of the RoboPol main sample have been observed for how many observing periods during the three seasons of observations.

Number of objects	Number of obs. periods
1	1
2	2
58	3
1	4

of rotations and their characteristic parameters depend on the time sampling is in preparation.

We select a duration of 50 days as an upper limit for the allowed time step between data points and split the data gaps larger than 50 days. In the following we refer to these subsets of data as *observing periods*. For each object, we treat each period as an individual data set when searching for rotations of the polarization angle. Since we are focusing on a study of variability, we include only periods that contain at least four data points. Following these criteria, each object is observed for at least one period, up to four periods (cf. Table 1), with a total sum of 183 periods. The durations of the observing periods range from 12–197 days (Fig. 2, panel a), consisting of 4–54 data points. The time steps during the selected periods range from 0.8–50 days (Fig. 2, panel b).

The electric vector position angle (EVPA), χ , is derived from the fractional Stokes parameters q and u (King et al. 2014, Eq. 6). The measured EVPA is limited to an interval of 180 deg. Therefore, differences between EVPA data points are measured modulo 180 deg and are, thus, ambiguous. Under the assumption of minimal variation, we shift the measured EVPA data points by multiples of 180 deg such that the difference between adjacent data points is always smaller than 90 deg. The following data analysis is entirely based on this shifted EVPA curve. Blinov et al. (2015, 2016a,b) used a different method that shifted data points only if the variability was significant. Kiehlmann et al. (2016) have shown that taking the uncertainties into consideration yields inconsistent results for the adjusted EVPA curve. We point out that the two different methods yield different EVPA curves only for the two sources RBPL J0841+7053 and RBPL J1058+5628. The rotations reported in Blinov et al. (2015, 2016a,b) are not affected by the choice of method.

3 DATA ANALYSIS

In this section, we define our quantitative criteria for a rotation of the EVPA. Then rotations in the RoboPol main sample are identified and characterized according to various parameters. Additionally, we investigate the behaviour of the polarization fraction during rotation and non-rotation periods.

3.1 Definition of an EVPA rotation

We use the method introduced by Kiehlmann et al. (2016) to identify periods of continuous EVPA rotations in the data and simulations consistently. This method identifies periods during which the EVPA changes continuously in one direction. Counter-rotations at the level of the uncertainties do

not interrupt a rotation. Only significant variability with a change of direction ends a detected rotation. A rotation between two data points χ_i, χ_j with uncertainties $\sigma_{\chi,i}, \sigma_{\chi,j}$ is considered significant when

$$|\chi_i - \chi_j| > \varsigma \sqrt{\sigma_{\chi,i}^2 + \sigma_{\chi,j}^2}. \quad (1)$$

The factor ς scales to what extent variability is interpreted as intrinsic or noise induced. We choose $\varsigma = 1$.

As we employ a method different from the one used in Blinov et al. (2015, 2016a,b) the rotations discussed here may differ from the ones previously reported for the RoboPol main sample. The method used here is likely to identify more rotations, as it decreases the chance of false non-detections when observational noise apparently changes the direction of the intrinsic variability. On the other hand, this method comes at the cost of increasing the chance of false positive detections. This could be the case when we observe intrinsic variability that is below the uncertainties. This intrinsic variability would break our definition of uni-directional EVPA variability, if it is a counter-rotation. But as it is insignificant, this variability is interpreted as noise and not as intrinsic and will not end a rotation. The advantages and disadvantages of both methods and consequences of the method selection will be discussed in more detail in a future paper. For this study it is merely important to use one method consistently.

Rotations are identified after adjusting the EVPA curve for the 180 deg ambiguity. We identify rotations for each observing period individually, i.e. we do not consider rotation to continue after a gap of ≥ 50 days. As in Blinov et al. (2015, 2016a,b), we accept only rotations that contain at least four data points. Blinov et al. (2015, 2016a,b) furthermore considered only rotations with large amplitudes $\Delta\chi \geq 90$ deg. We do not apply a cut on the amplitude in general. In the following we discuss results for two schemes of identifying rotations: first, accepting all rotations with arbitrary amplitudes and, second, accepting only rotations with large amplitudes ($\Delta\chi \geq 90$ deg). We designate the former as *rotations* and the latter as *large rotations*. Rotations with amplitudes $\Delta\chi < 90$ deg are referred to as *small rotations*. Figure 1 shows an example of identified rotation periods for RoboPol object RBPL J1800+7828. Red data points mark periods of large rotations, blue points mark small rotations, and black points are not identified as part of a rotation.

The identification of rotations depends on the sampling and the measurement uncertainties. There is always a chance of identifying rotations wrongly due to the uncertainties or to miss them due to uncertainties or insufficient time sampling. Therefore, in the comparison of data and models the time sampling and measurement uncertainties, as shown in Fig. 2, have to be accounted for in the model simulations.

3.2 Characteristics of the rotations

Following the criteria above, we have identified 343 rotations in the three seasons of the RoboPol main sample observations, 98 of which are large rotations (Table 2). The third column in Table 2 shows the frequency of rotations per 100 days, averaged over the entire sample. This estimate is based on the sum of the observing periods $T_{\text{obs,tot}} = 21783.7$ days. Durations of the observing periods are not

Table 2. Absolute number and estimated frequency of rotations observed in the RoboPol main sample and number of sources showing rotations with certain amplitudes.

Amplitudes	Number of rotations		Number of sources	
	absolute	per 100 days	absolute	relative
all	343	1.57	61	98%
≥ 90 deg	98	0.45	43	69%
≥ 180 deg	25	0.11	15	24%
≥ 270 deg	3	0.01	3	5%
≥ 360 deg	1	<0.01	1	2%

taken into account. Therefore, the estimated frequencies depend not only on the intrinsic behaviour of the sources, but also on the observing schedule.

We measure four parameters that characterize the rotations. The *amplitude* of a rotation is $\Delta\chi = \max\chi_i - \min\chi_i$, where χ_i are the data points of an identified rotation. The *duration* T_{rot} is the time passing between the start and end of the rotation. We estimate the average *rotation rate* through $\Delta\chi T_{\text{rot}}$. And we use the *variation estimator* s_χ defined in Kiehlmann et al. (2016) to quantify the smoothness of the EVPA curve:

$$s_\chi = \langle |s_i| \rangle = \left\langle \left| \left\langle \left(\frac{\Delta\chi}{\Delta t} \right)_i \right\rangle - \left\langle \left\langle \left(\frac{\Delta\chi}{\Delta t} \right) \right\rangle \right| \right\rangle \quad (2)$$

$$\text{with } \left(\frac{\Delta\chi}{\Delta t} \right)_i = \frac{\chi_i - \chi_{i-1}}{t_i - t_{i-1}}, \quad (3)$$

where $\langle \cdot \rangle$ denotes the mean over all i . A larger value reflects stronger variability and a less smooth curve.

3.2.1 Limits and biases in the rotation parameters

The variation estimator is affected by observational errors and intrinsic curvature of the EVPA curve. Both biases increase s_χ (Kiehlmann et al. 2016). The rotation amplitude, duration and rate are affected by the time sampling and limited observing periods. The measured rotation amplitude and duration are generally lower limits. A detected rotation probably starts between the first data point of the measured rotation and the preceding data point and continues between the last and the following data point. Accordingly, the estimates of the average rotation rate are affected and the actual values could be larger or smaller. The uncertainties of these measurements depend on the time sampling and the source intrinsic variability.

Most critical are cases in which the detected rotation starts or ends with the observing period. The actual rotation could extend far beyond this period. The limited duration of the observing periods (Fig. 2, panel a) puts a strict constraint on the measurable duration of rotations and the amplitudes and durations may as a result be underestimated and rotation rates wrongly estimated accordingly. The majority of rotations (72%) is fully covered by the corresponding observing periods. The measured parameters of these rotations are solely limited by the limited time sampling. 26% of the rotations either start or end with the observing period and eight identified rotations cover the entire period, during which they are observed.

The estimated rotation parameters are generally limited or biased and depend not only on the intrinsic variability of the sources but also on the scheduling of observations and

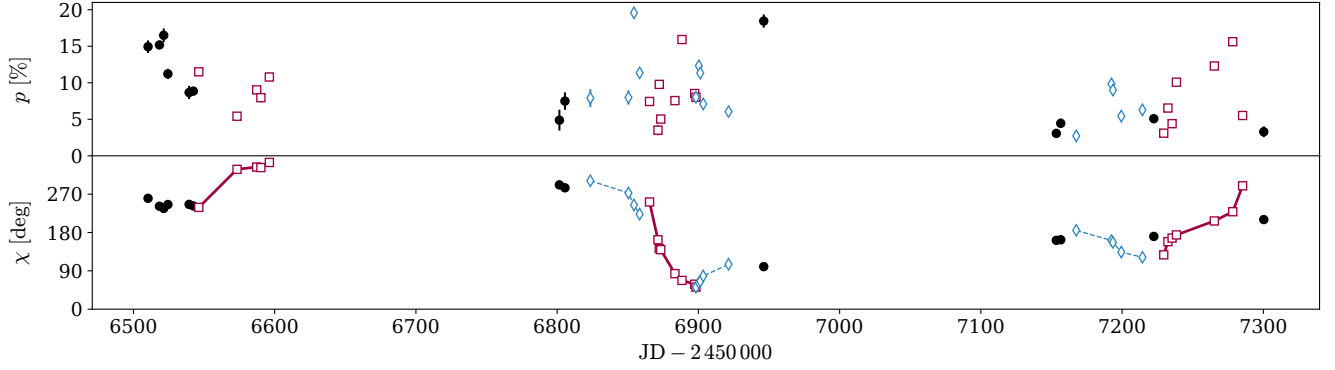


Figure 1. Polarization fraction and EVPA of RBPL J1800+7828. Coloured data points, connected by lines mark periods of small ($\Delta\chi < 90$ deg, blue diamonds, dashed lines) and large ($\Delta\chi \geq 90$ deg, red squares, solid lines) rotations. Black points are not part of a rotation period.

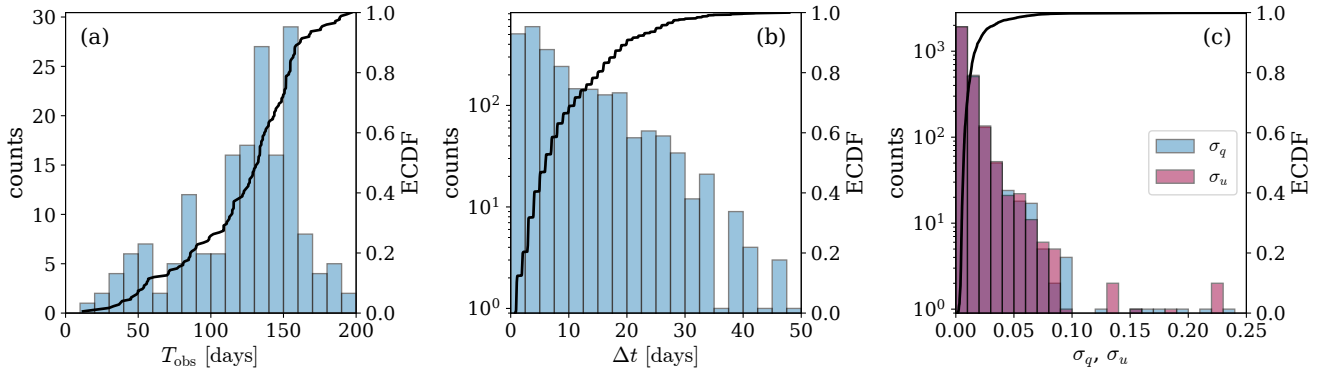


Figure 2. Empirical distributions based on the RoboPol main sample used for the random simulations. *Panel a:* Duration of observing periods. *Panel b:* Time steps during observing periods. *Panel c:* Uncertainties of the fractional Stokes parameters q and u (blue and red histogram). The empirical cumulative distribution function (ECDF, black line) is based on the combined uncertainties of q and u .

Table 3. Minimum, maximum, mean, and median values of the rotation amplitudes (*col. 2*), durations (*col. 3*), rates (*col. 4*), and variation estimators (*col. 5*) observed in the RoboPol main sample.

	$\Delta\chi$ deg	T_{rot} days	$\Delta\chi T_{\text{rot}}$ degday	s_χ degday
Min.:	4	3	0.1	0.1
Max.:	423	120	52.1	26.8
Mean:	70	33	3.1	3.3
Median:	49	29	1.9	1.9

the measurement uncertainties. In the comparison of the data and simulations these limitations have to be accounted for by reproducing the time sampling, observing periods, and uncertainties of the data in the simulations.

3.2.2 Distributions of the rotation parameter

Figures 3 to 6 show the distributions of the four parameters characterizing the rotations that are found in the RoboPol

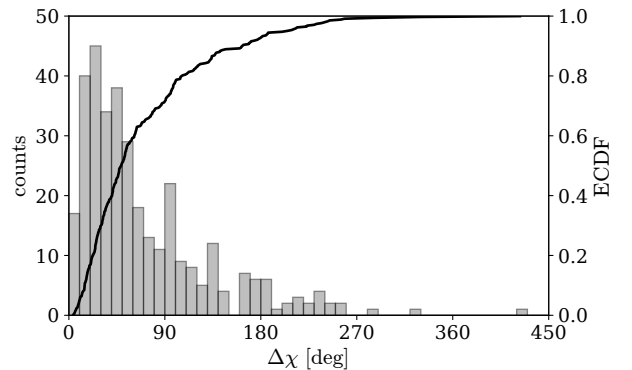


Figure 3. Distribution of rotation amplitudes in the RoboPol main sample.

main sample. Minimum, maximum, mean, and median values of the distributions are given in Table 3.

The large rotations have on average slightly longer durations than the small rotations (Fig. 4). We use a two-sample

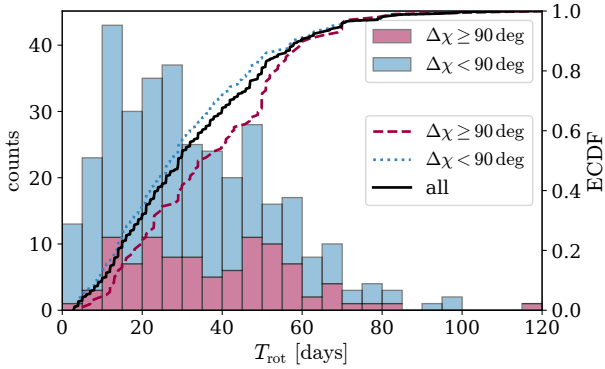


Figure 4. Distribution of rotation durations in the RoboPol main sample. The stacked histograms are based on the large (red) and small (blue) rotations only, the coloured ECDFs accordingly. The black ECDF is based on all rotations.

Kolmogorov–Smirnov (KS) test to test whether the durations of the small rotations and the large rotations come from the same distribution. This hypothesis cannot be rejected at the 1% significance level or lower (p-value: 0.01), showing there is no significant difference between the durations of small and of large rotations. This implies that long-lasting rotations do not necessarily correlate with large rotation amplitudes. Instead, it is mostly the rotation rate that should affect the amplitude. Indeed, we find that the rotation rates of the population of large rotations are on average higher (Fig. 5) and the KS test indicates a significant difference between the two distributions (p-value: $\sim 10^{-26}$). Having the rotation amplitudes depend more on the rotation rate than on the rotation duration could be an artefact of the observations. As the observing periods are limited, larger rotations have to be produced by faster rotations.

28% of the measured amplitudes and durations are lower limits. Therefore, the distributions shown in Figs. 3 and 4 depend on the sampling of the observations. Likely, the intrinsic distributions are partially shifted to higher values. The distribution of the average rotation rates are affected accordingly. 28% of the measurements may be over- or underestimated, if the rotation rate during the rotations is variable.

Due to the 180 deg ambiguity, EVPA variability can only be measured correctly if the EVPA changes by less than 90 deg between two data points. Therefore, the median observation cadence of 6 days corresponds to an upper limit for the detectable rotation rates of $\lesssim 15$ deg/day. The distribution of rotation rates is thus limited by the sampling cadence. Figure 5 is cropped after the second fastest rotation with a rate of 21 deg/day. The fastest rotation with a rate of 52 deg/day occurs in RBPL J2202+4216, showing a 259 deg rotation within five days, over five data points. It is shown in Fig. 2 of Blinov et al. (2015)².

Figure 6 shows the distribution of the EVPA variation estimator. The two distributions based on the large and the short rotations are significantly different as indicated by a

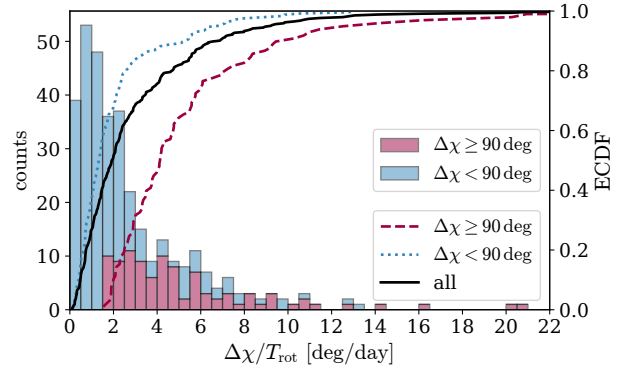


Figure 5. Distribution of rotation rates in the RoboPol main sample. The stacked histograms are based on the large (red) and small (blue) rotations only, the coloured ECDFs accordingly. The black ECDF is based on all rotations.

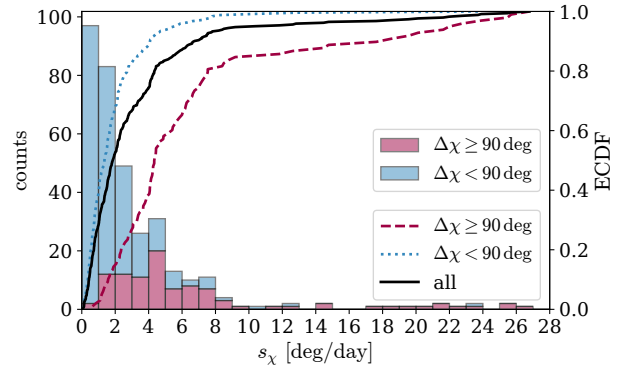


Figure 6. Distribution of the rotation variability in the RoboPol main sample. The stacked histograms are based on the large (red) and small (blue) rotations only, the coloured ECDFs accordingly. The black ECDF is based on all rotations.

two-sample KS test (p-value: $\sim 10^{-26}$). The large rotations are on average more erratic than the small rotations. The variation estimator is, per definition (cf. Eq. 2), independent of the rotation rate, assuming a constant rate. It is increased by erratic variability superimposed on a secular trend, non-linear trends, and measurement uncertainties, whereas the latter two are regarded as biases (Kiehlmann et al. 2016). Given the adaptive scheduling scheme of the RoboPol observations, large rotations are more densely sampled in time than small rotations, as stronger variability led to intensified monitoring. Testing the two biases of the variation estimator for a dependence on the number of data points, we find that indeed both biases increase with larger numbers of data points. The effect of this dependence is at least one order of magnitude lower than the difference between the two distributions shown in Fig. 6. Therefore, these biases cannot explain why large rotations are on average more erratic than small rotations.

In the following section we investigate potential relations between different rotation parameters taking the lower limit into consideration.

² This rotation is identically found with both methodologies used to identify rotations here and in Blinov et al. (2015).

3.2.3 Relations between the rotation parameters

Figure 7 shows the rotation amplitude plotted against its duration and rate. Small rotations are marked by blue dots, large rotations by red squares. Open symbols mark the 28% of the rotations that were limited by the observing periods. These measurements are lower limits for the amplitudes and durations and uncertain for the rotation rate (cf. Section 3.2.1).

Rotations of any amplitude cover a large range of durations and rotation rates. We use a generalized version of the Kendall rank correlation coefficient τ as described by Feigelson & Babu (2012, Chapter 10.4.1, Eq. 10.23), which accounts for censored data. We treat the amplitudes and durations that are limited by the observing periods as lower limits. Rotation rates are treated as exact measurements as they can be either over- or underestimated. The correlation coefficients indicate that the rotation amplitude depends slightly more strongly on the rate ($\tau = 0.38$) than on the duration ($\tau = 0.32$). When considering only the measurements and not the lower limits, the stronger dependence of the rotation amplitude on the rotation rate ($\tau = 0.5$) rather than on the duration ($\tau = 0.18$) becomes more evident. These results are consistent with the discussion of the distributions in the previous section and indicate that the dependence of the amplitude on the rate rather than the duration is an intrinsic effect and not a sampling artefact.

Figure 8 shows the variation estimator plotted against the rotation duration, amplitude, and rate. We use the generalized Kendall rank correlation coefficient τ to test these pairs of parameters for correlations, considering the amplitudes and durations limited by the observing periods as lower limits. The correlation coefficient $\tau = -0.15$ does not indicate a strong relation between the variation estimator and the duration (panel a). On the other hand, $\tau = 0.36$ for the amplitude and $\tau = 0.56$ for the rotation rate indicate a relation between these parameters and the variation estimator. Thus, rotations with larger amplitudes are on average more variable, i.e., less smooth. Accordingly, higher rotation rates lead on average to stronger variability.

This behaviour would be expected from a stochastic process. To produce larger rotations or higher rotation rates, stronger variability is needed in the EVPA, which increases the erratic behaviour of the rotations (Kiehlmann et al. 2016). Consistently, strong erratic variability is less likely to produce a continuous rotation over a long period. This behaviour is indicated in the negative sign of the weak correlation between variation estimator and duration (cf. Fig. 8, panel a). We test whether these rotations follow a stochastic process in Section 3.2.3.

3.3 Polarization fraction during rotation and non-rotation periods

We test whether the polarization fraction behaves differently during rotations and non-rotation periods. For each object we calculate the mean and standard deviation of the polarization fraction during the rotation periods, $\langle p \rangle^{\text{rot}}$ and σp^{rot} , based on all data point that are part of a rotation period. And we calculate these values, $\langle p \rangle^{\text{non-rot}}$ and $\sigma p^{\text{non-rot}}$, for the non-rotation periods, which are all data points that are not identified as part of a rotation. Then,

we calculate the ratio of the mean polarization fraction during the rotation and non-rotation periods, and the ratio of the standard deviation accordingly. We perform this analysis in two ways. First, we consider *all* rotations. In the example of Fig. 1 all coloured data points (red and blue) contribute to $\langle p \rangle^{\text{rot}}$ and σp^{rot} and black data points contribute to $\langle p \rangle^{\text{non-rot}}$ and $\sigma p^{\text{non-rot}}$. Second, we consider only *large* rotations. Here, only red data points contribute to $\langle p \rangle^{\text{rot}}$ and σp^{rot} , while black and blue data points contribute to $\langle p \rangle^{\text{non-rot}}$ and $\sigma p^{\text{non-rot}}$.

The blue histograms and ECDFs in Fig. 9 show the distributions of the ratios of polarization means and ratios of polarization standard deviations, based on all identified rotations in the RoboPol main sample. On average, the mean and standard deviation of the polarization fraction is higher during the rotation periods than during the non-rotation periods. The red distributions in Fig. 9 consider only large rotations as rotation periods. In this case, the mean polarization fraction is on average lower during the rotation periods than during the non-rotation periods and similarly the standard deviation of the polarization fraction. This comparison indicates that the large rotations exhibit a lower and less variable polarization fraction, whereas the small rotations mostly show a higher and more variable polarization fraction. Similar results were reported in Blinov et al. (2016a), where this analysis was based on maximum-likelihood estimates of the mean and the modulation index of the polarization fraction during rotations and non-rotations.

4 RANDOM WALK SIMULATIONS

In Section 3.2.3 we argued that the observed relation between the rotation variability and the amplitude as well as the relation between the variability and the duration can be explained by a stochastic process. In the following we test whether these data are consistent with a basic random walk process that emulates a turbulent flow in a turbulent magnetic field structure.

Turbulence may arise from current-driven instabilities (e.g. Nalewajko & Begelman 2012) and transverse velocity gradients in the flow (e.g. Vlahakis & Königl 2004). Kiehlmann et al. (2016) describe three basic random walk processes, using cells that randomly change their properties to model the turbulence. They show that the three processes cannot be distinguished from one another. The only difference is the requirement of slightly different values for the main model parameters to reproduce the same data. Therefore, we limit our simulations and analysis to the “simple Q, U random walk process”, which we briefly outline in the following.

We create N_{cell} cells. Each cell is assumed to contain a randomly oriented, uniform magnetic field. Thus, the synchrotron emission from each cell is maximally polarized, $p_{\text{max}} \approx 0.72$, assuming an electron energy spectrum with index 2.5 (Longair 2011, p. 217), and has a randomly oriented EVPA. Additionally, we assume that each cell emits an equal amount of radiation. Following Kiehlmann et al. (2016), we directly model the Stokes parameters Q_i and U_i for each cell i through drawing two random numbers $\hat{Q}_i \sim \mathcal{N}(0, 1)$, $\hat{U}_i \sim \mathcal{N}(0, 1)$ from a normal distribution. The relative Stokes

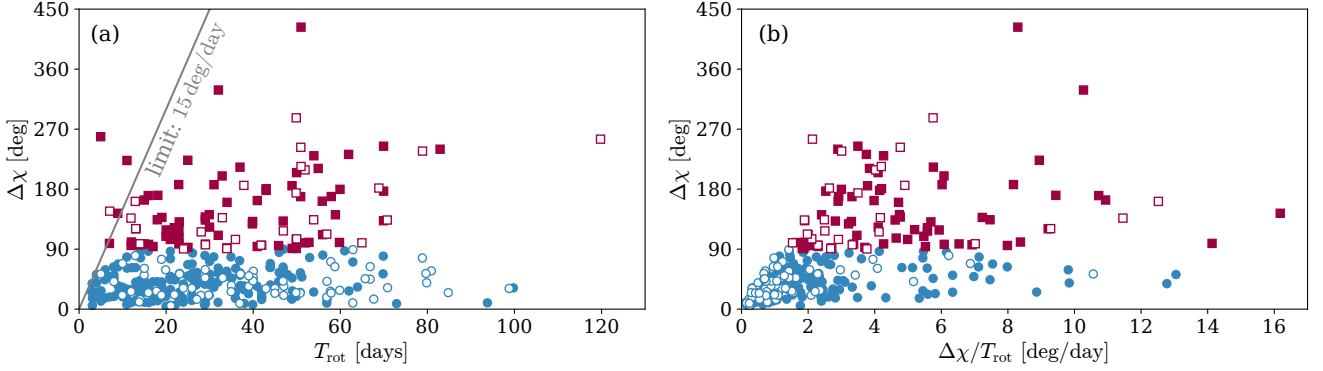


Figure 7. Dependence of the rotation amplitude on the rotation duration (*panel a*) and the rotation rate (*panel b*). Blue dots show small ($\Delta\chi < 90$ deg), red squares large rotations ($\Delta\chi \geq 90$ deg). Open symbols indicate lower limits for the amplitude and duration and uncertain rotation rates due to the limited observing periods. The grey line marks the upper limit of measurable rotation rates, based on the median time sampling.

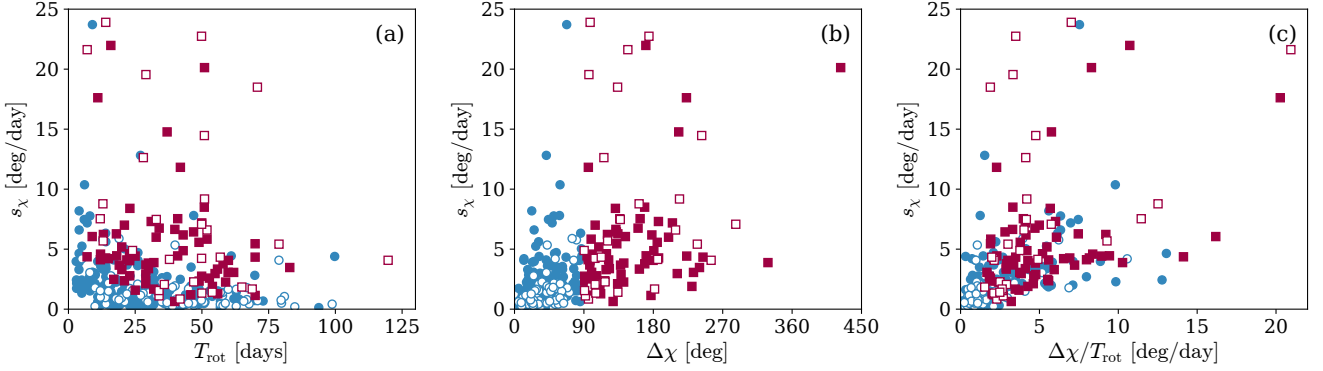


Figure 8. Dependence of the rotation variation estimator on the amplitude (*panel a*), duration (*panel b*), and rate (*panel c*). Symbols are as in Fig. 7.

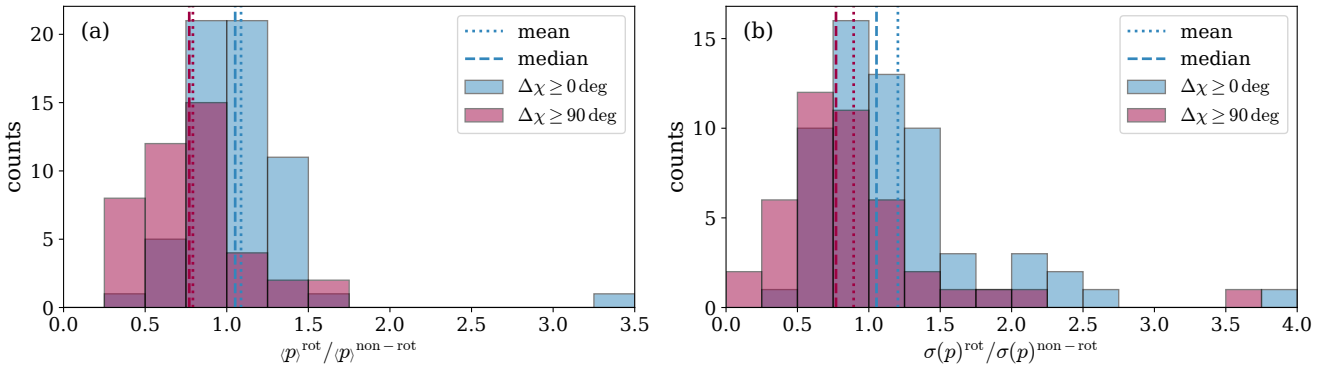


Figure 9. Distributions of the ratio between the polarization fraction mean during rotations and during non-rotations (*panel a*) and the standard deviation of the polarization fraction accordingly (*panel b*), based on the RoboPol main sample. The blue histograms and ECDFs consider all rotations of arbitrary amplitudes, the red distributions accepted only rotations of amplitudes $\Delta\chi \geq 90$ deg. The dotted and dashed lines show means and medians of the corresponding distributions.

parameters are calculated from these random numbers as

$$q_i = \frac{Q_i}{I} \quad \text{with} \quad Q_i = \frac{\hat{Q}_i}{\sqrt{\hat{Q}_i^2 + \hat{U}_i^2}} \cdot I_i \cdot m_{l,\max}, \quad (4)$$

$$u_i = \frac{U_i}{I} \quad \text{with} \quad U_i = \frac{\hat{U}_i}{\sqrt{\hat{Q}_i^2 + \hat{U}_i^2}} \cdot I_i \cdot m_{l,\max}, \quad (5)$$

which ensures the maximum polarization and equal intensity $I_i = \frac{I}{N_{\text{cells}}}$ for all cells, where $I = \sum_{i=1}^{N_{\text{cells}}} I_i$ is the total intensity. As EVPA and polarization fraction are independent of the total intensity, it is set to $I = 1$. The polarization fraction p and the EVPA χ are calculated from the summed Stokes parameters $q = \sum_{i=1}^{N_{\text{cells}}} q_i$ and u accordingly through

$$p = \sqrt{q^2 + u^2}, \quad (6)$$

$$\chi = \frac{1}{2} \arctan \frac{u}{q}, \quad (7)$$

using the `atan2` definition of the arctangent that returns the correct quadrant of the angle in the range -180 deg, 180 deg. At each time step several cells are randomly selected and their properties are changed randomly according to the previous formalism. The cell variation rate n_{var} , sets the number of cells that change each unit time step. We point out that we study and model the variability in the observer's frame. The simulations are implicitly assumed to be affected by the same Doppler factor and redshift distribution as the data. Modelled cell variation rates are not source intrinsic rates.

As discussed in Section 3.2.1 the parameters used to characterize rotations are affected by time sampling and measurement uncertainties. For a reliable comparison of data and simulations the simulations need to be affected by the same biases. Therefore, we simulate time steps and observational noise similar to the observed data. Random simulation time steps, Δt_i , are drawn from the ECDF of the observation time steps (Fig. 2, panel a) and simulation durations, T_{sim} , are randomly drawn from the ECDF of observing periods (Fig. 2, panel c). We simulate observational errors through randomly drawing uncertainties $\sigma_{q,t}$ from the ECDF of the combined, observed uncertainties of q and u (Fig. 2, panel c) for each simulation time t . In the simulations we set $\sigma_{q,t} = \sigma_{u,t}$. The random errors $q_{\text{err},t}$, $u_{\text{err},t}$ are drawn from a normal distribution $\mathcal{N}(0, \sigma_{u,t})$ and added to the summed q and u for every time step before calculating the polarization fraction and EVPA.

Before testing this model against the RoboPol main sample data in Section 5, we discuss general dependencies on the model parameters N_{cells} and n_{var} . Figure 5 in Kiehlmann et al. (2016) depicts the relation between the model parameters and the mean and standard deviation of the polarization fraction. We limit the tested parameter space according to the polarization fraction observed in the RoboPol main sample. The observed mean polarization fraction ranges from 1% to 24%, the standard deviation from 0.6% to 12%. With 20 cells a mean polarization fraction of $\sim 15\%$ is expected, though higher values may occur (Kiehlmann et al. 2016, Fig. 5). The lowest mean and standard deviation observed in the polarization fraction may be produced by up to 1000 cells. We test the following parameter space:

Numbers of cells: $N_{\text{cells}} \in 20, 40, \dots, 1000$,
Cell variation rates: $n_{\text{var}} \in 2, 4, \dots, 100$ cells per day.

4.1 Expected number of rotations

For each parameter combination we run 500 simulations³ with total times T_{sim} randomly drawn from the ECDF of observing periods (Fig. 2, panel b). We count the identified rotations over the summed total time of each set of 500 simulations. Figure 10 shows the number of rotations per 100 days expected from this random walk process depending on the model parameters for different minimum rotation amplitudes.

Considering rotations with arbitrary amplitudes, the left panel of Fig. 10 suggests that there is a ratio of number of cells and cell variation rates that increases the frequency of rotations. Too many cells or too small variation rates decrease the frequency of rotations as it becomes less probable to find significant variability in the EVPA. On the other hand, very few cells or high variation rates decrease the frequency of rotations as the EVPA becomes more erratic. The frequency of 1.57 rotations per 100 days observed in the RoboPol sample (Table 2) suggests that the sources should be located at small numbers of cells $N_{\text{cells}} \lesssim 100$ in the model parameter space, if they follow this random walk process.

Considering large rotations, the middle panel of Fig. 10 shows that lower variation rates and larger numbers of cells decrease the frequency of large rotations. Both effects reduce the variability of the EVPA, which is needed to produce large rotations. The frequency of 0.45 large rotations per 100 days in the RoboPol sample (Table 2) indicates that these sources require $N_{\text{cells}} \gtrsim 100$ and that approximately 2% of the cells vary per day.

The discrepancy between the location of the sources in the parameter space, estimated on the basis of all rotations with arbitrary amplitudes or on the basis of large rotations, implies that not all sources can be located in the same region of the parameter space if they follow this model.

4.2 Model parameter dependence

We use the simulations described in Section 4.1 to estimate expectation values for the rotation parameters – amplitude, duration, rate, and variability – and investigate their dependence on the model parameters.

As for the frequency of rotations in Fig. 10, we find similar dependencies between the rotation parameters and the model parameters. Rotation amplitudes, rates, and variation estimators increase with fewer cells and higher cell variation rates, which increases the variability of the EVPA. The longest rotation durations are obtained at a certain ratio between number of cells and cell variation rate. Too low or too high variation rates decrease on average the rotation duration. These dependencies show that the rotation parameters

³ With 50 test values for the number of cells and 50 values for the cell variation rate, we test 2500 points in the parameter space. Due to computer time restrictions we limit the number of simulations at each point to 500, which gives a total of 1 250 000 simulations.

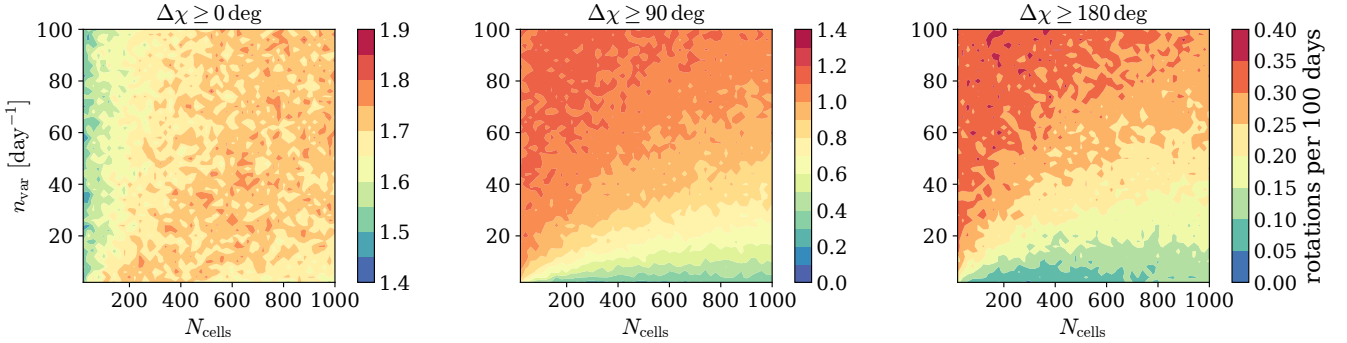


Figure 10. Expected number of rotations per 100 days with arbitrary amplitudes (*left panel*), amplitudes larger than 90 deg (*mid panel*), and amplitudes larger than 180 deg (*right panel*).

and particularly the combination of the rotation parameters allow sources to be located in the model parameter space.

In the tested parameter space we identify rotations with amplitudes up to 730 deg, durations up to 194 days, rates up to 99 deg/day, and variation estimators up to 61 deg/day. These values are not general results of the random walk process, but depend on the time sampling, observing periods, and EVPA uncertainties of the RoboPol observations. Nonetheless, they show that all rotation parameters observed in the RoboPol main sample (Figs. 3 to 6) can be produced by the random walk process within the tested model parameter space.

4.3 Rotation parameter relations

In Section 3.2.3 we have discussed potential relations between the parameters that characterize the rotations in the RoboPol main sample. We use the simulations described in Section 4.1 to test whether these dependencies are consistent with the random walk process. From the simulations run at a particular point in the model parameter space we randomly select 343 rotations, the same number we have observed in the data. We find that the random walk process can produce a set of rotations that occupy roughly the same rotation parameter space as in Figs. 7 and 8 and show similar relations between the rotation parameters. These simulations are not directly comparable to the data, as the RoboPol sources may be located at different regions of the model parameter space. Nevertheless, these results indicate that *the relations between the rotation parameters found in the data are consistent with a random walk process*. We discuss a thorough test between data and simulations in Section 5.

4.4 Expected polarization fraction during rotations and non-rotations

In Fig. 9 we have shown that the polarization fraction in the RoboPol main sample is on average lower during large rotations than during small and non-rotations. Here we test whether in the random walk model the mean and the standard deviation of the polarization fraction change between periods that are perceived as rotations and non-rotations.

The data-based results are affected by sparse time sampling. Rotation and non-rotation periods may consist of only

a few data points, yielding unreliable estimates of the mean and standard deviation and the ratios thereof. In contrast, here we use reliable estimates by simulating long time series with $T_{\text{sim}} = 500\,000$ days. For each parameter combination given in Section 4 we run a long simulation with time steps randomly drawn from the distribution shown in panel b of Fig. 2. For each of the 2500 simulations we identify rotations and calculate the ratios of the mean polarization fraction (or standard deviation) during rotation and non-rotation periods, as described in Section 3.3. The model results are shown in Fig. 11.

The left panel shows the ratio of the mean polarization fraction during apparent rotations and non-rotation periods. Considering only large rotations (red distribution), the mean polarization fraction is lower during apparent rotations than during non-rotations, ranging down to half the mean polarization fraction of non-rotation periods. Considering rotations with arbitrary amplitudes (blue distribution), the difference in the mean polarization fraction is not as pronounced as for large rotations. Still, the mean polarization fraction during apparent rotations is mostly below the mean polarization fraction of non-rotation periods.

An apparent EVPA rotation occurs when various cells vary their magnetic field orientation by chance, such that the net EVPA changes continuously in one direction. In principle, a single, gradually changing cell can cause an apparent rotation, when the polarization of all other cells roughly cancels out. The polarization fraction is high when many cells accidentally align. In this configuration, many cells are required to change accordingly to produce an apparent rotation. Thus, it is more likely that a few cells cause large rotations, while the other cells are unaligned and their polarization cancels out. Consequentially, by picking out periods that show apparent large rotations we are more likely to select low polarized periods. When selecting apparent rotations with arbitrary amplitudes, the difference in the mean polarization fraction between rotation and non-rotation periods becomes less pronounced for two reasons. First, the fraction of data points selected as part of rotations with arbitrary amplitudes is significantly higher than selecting only large rotations. For example, 66% of the RoboPol data points are part of rotations with arbitrary amplitudes, while only 22% contribute to large rotations. Therefore, the ratio of the mean polarization fraction is closer to one, when

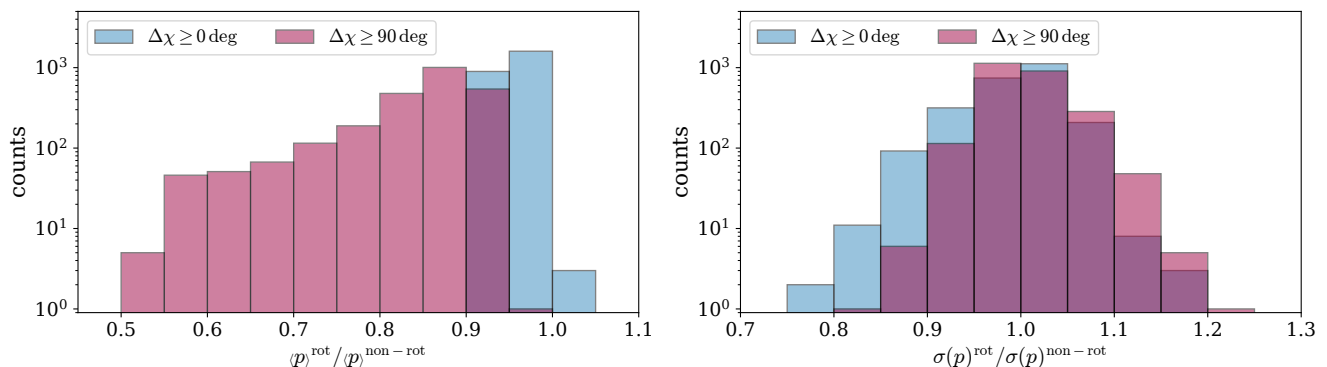


Figure 11. *Left panel:* Distribution of the ratio of the mean polarization fraction during rotations to non-rotation periods. *Right panel:* Distribution of the ratio of the polarization fraction standard deviation during rotations to non-rotation periods. The distributions are based on all simulations covering the entire tested parameter space with $T_{\text{sim}} = 500\,000$ days.

considering all rotations. Second, small rotations may occur with more cells aligned, i.e., higher polarization fraction, whereas it becomes less likely that many cells align subsequently to produce a large rotation. Consequentially, small rotations are potentially more polarized than large rotations.

The right panel of Fig. 11 shows the ratio of the standard deviation of the polarization fraction during apparent rotations and non-rotation periods. The standard deviation may be larger or smaller during apparent rotations than in non-rotation periods. The distributions of the ratio peak around 1.0 in both cases, considering rotations with large amplitudes (red distribution) and arbitrary amplitudes (blue distribution).

By selecting periods of polarization data that apparently show a characteristic behaviour in the polarization angle, we select out periods that also differ in the polarization fraction compared to the rest of the data. *A difference in the polarization fraction between rotation and non-rotation periods does not necessarily indicate a different process during these periods, nor does it contradict a random walk process.* In fact, it is consistent with a random walk process and is the result of a selection effect. In particular, the observation that periods of large rotations in the RoboPol main sample are on average less polarized and less variable in the polarization fraction than during the non-rotation periods does not reject the random walk hypothesis.

The observed distributions in Fig. 9 and the simulation results in Fig. 11 are not directly comparable for two reasons. First, we have simulated long time series with $T_{\text{sim}} = 500\,000$ days to avoid unreliable estimates of the mean and standard deviation of the polarization fraction. Repeating the simulations with T_{sim} randomly drawn from panel a of Fig. 2, the distributions shown in Fig. 11 peak at value one, but extend to much higher values. This shows that a higher mean polarization fraction during rotation periods is possible, but is an artefact of a low number of data points. Second, the distributions in Fig. 11 result from simulations at 2500 points in the model parameter space, equally distributed over the parameter space. It is not known a priori, where the RoboPol sources are located in the parameter space if they can be described by this random walk process.

A direct comparison of simulations and the RoboPol data is discussed in Section 5.

4.5 Mean polarization fraction and rotation rate

Blinov et al. (2016a) report a correlation between $\langle p \rangle^{\text{rot}} \langle p \rangle^{\text{non-rot}}$ and the logarithm of the source intrinsic rotation rate with a correlation coefficient -0.66 and slope -0.19 ± 0.07 , based on 16 sources for which Doppler factor and redshift were available. We have shown in Section 4.4 that large rotations in the random walk model are on average less polarized than non-rotation periods. With a relation between the rotation rate and amplitude and a dependence between amplitude and the mean polarization fraction, the relation between $\langle p \rangle^{\text{rot}} \langle p \rangle^{\text{non-rot}}$ and the rotation rate could be a result of a random walk process.

To test whether this relation is consistent with a random walk, we select one of the long simulations with $T_{\text{sim}} = 500\,000$ days described in Section 4, which covers one point in the model parameter space. We randomly pick 16 rotations, estimate $\langle p \rangle^{\text{rot}} \langle p \rangle^{\text{non-rot}}$ and the rotation rate for each one, and run a linear regression over the mean polarization fraction ratio and the logarithm of the rotation rate. Repeating this step for 20 000 iterations, we estimate the probability that the linear regression yields a slope within the range -0.19 ± 0.07 and a correlation coefficient < -0.66 . We repeat this analysis at various points in the model parameter space. Depending on the position in the parameter space the probability of measuring a similar slope as for the RoboPol data ranges between 14% and 20%. The probability of measuring a correlation coefficient more extreme than for the RoboPol data ranges from 1% to 7%.

While the simulations are not directly comparable to the RoboPol data due to the longer time-scale they cover and the unknown location of the RoboPol sources in the model parameter space, these results show that *a relation between the mean polarization fraction ratio and the rotation rate does not reject the random walk hypothesis.*

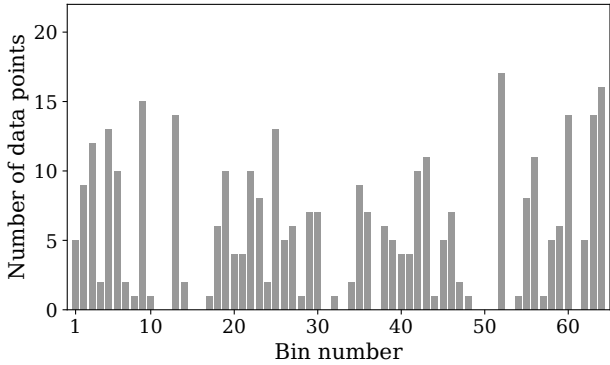


Figure 12. Number of data point contained in each bin of the rotation parameter space amplified by amplitudes, durations, and variability.

5 TESTING SIMULATIONS AGAINST DATA

In this section we discuss a method to constrain the model parameter space. Then we test simulations against the data of the RoboPol main sample; focusing first on the characteristics of the EVPA rotations, second on the polarization fraction, and third on the observed number of rotations.

5.1 Constraining the model parameter space

We characterize rotations by three independent parameters: amplitude, duration, and variation estimator. We divide this three-dimensional parameter space by the following limits:

$$\begin{aligned} \Delta\chi: & 0, 26, 49, 90, 423 \text{ deg}, \\ T_{\text{rot}}: & 0, 16, 29, 47, 120 \text{ days}, \\ s_{\chi}: & 0, 0.8, 1.8, 4.1, 27 \text{ degday}, \end{aligned}$$

yielding four bins along each dimension and a total of 64 bins. The bin ranges were chosen such that (i) most of the bins contain data points (52 out of 64) and (ii) the filled bins contain on average more than six data points. The upper limits are based on the largest values observed in the RoboPol sample. Fig. 12 shows the number of data points for each bin, ranging between 1 and 17 for the filled bins.

In Section 4.2 we have argued that the rotations resulting from the random walk process depend on the number of cells N_{cells} and the cell variation rate n_{var} . These model parameters are a priori unknown for all sources in the RoboPol main sample. To compare our simulations against the observations, we need to limit the model parameter space. Therefore we assume that the number of cells and the cell variation rate of all sources follow predefined distributions, which are also a priori unknown. For the following explanation we assume that both parameters follow a log-normal distribution, $N_{\text{cells}} \sim \mathcal{LNM}_{C,S}$, $n_{\text{var}} \sim \mathcal{LNM}_{v,S_v}$, with the corresponding distribution means M_C , M_v and standard deviations S_C , S_v . The log-normal distribution is a natural choice for both parameters as it gives only positive values, but it is not physically justified. We discuss alternative test-distributions later. The distribution parameters M_C , S_C , M_v , S_v are a priori unknown. We keep them as variables in the following minimization procedure:

(i) Values for M_C , S_C , M_v , S_v are randomly picked.

(ii) A random source sample is constructed picking 62 pairs of model parameters, $N_{\text{cells}}, n_{\text{var}}, i=1, \dots, 62$, from $\mathcal{LNM}_{C,S}$ and \mathcal{LNM}_{v,S_v} .

(iii) A sample of simulated EVPA curves is constructed. Here, we reproduce the same number of observing periods as in the RoboPol main sample (Table 1), running four simulations for one object, three simulations for 58 objects, two simulations for two objects, and one simulation for the remaining object. The total time T_{sim} of each simulation is randomly drawn from the ECDF of observing periods (Fig. 2, panel a).

(iv) Rotations are identified in the simulation sample and the corresponding rotation parameters are measured. The rotations falling into each bin $N_{\text{sim},i}$ are counted.

(v) Steps (ii) to (iv) are repeated for N_{iter} iterations. Each time the number of rotations per bin is stored.

(vi) For each bin i we calculate the expected number of rotations $\bar{N}_{\text{sim},i}$ and the corresponding standard deviation $S_{\text{sim},i}$ based on the N_{iter} iterations. Then we calculate the statistics

$$\chi^2_{M_C, S_C, M_v, S_v} = \sum_{i=1}^{64} \frac{(\bar{N}_{\text{sim},i} - N_{\text{obs},i})^2}{S_{\text{sim},i}}, \quad (8)$$

where $N_{\text{obs},i}$ is the number of rotations of the RoboPol sample in each bin. The sum is over all 64 bins.

For step (v) we choose $N_{\text{iter}} = 500$. The number of iterations is chosen relatively low to limit the calculation time, but large enough to get reliable estimates of $\bar{N}_{\text{sim},i}$, $S_{\text{sim},i}$, and $\chi^2_{M_C, S_C, M_v, S_v}$.

We run a minimization process over steps (i) to (vi) to find the optimal distribution parameters M_C , S_C , M_v , S_v to produce a set of rotations comparable to the ones found in the RoboPol main sample. For the minimization we use the *Differential Evolution* algorithm by Storn & Price (1997) implemented in the `scipy` (v. 0.18.1) python package⁴.

5.1.1 Test distributions

As explained in the previous section, we assume that the number of cells and the cell variation rate follow a priori unknown distributions. We test various generic distribution types for both parameters: (a) uniform distribution \mathcal{UL}, U with lower limit L and upper limit U , (b) log-normal distribution \mathcal{LNM}, S with mean M and standard deviation S , and (c) normal distribution $\mathcal{N}_{\text{trunc}}, M, S$ truncated such that all values are larger than zero, where M and S are the mean and standard deviation of the corresponding non-truncated normal distribution. Values drawn for the number of cells are rounded up to the next integer. For the cell variation rate we additionally test a truncated power-law distribution \mathcal{PL}, L, U with index α and lower and upper limits L and U . A power-law distribution may be physically justified, assuming that the cell variation rate corresponds to the flow speed and, thus, to the Lorentz factor, which is found to follow a power-law distribution (Lister & Marscher 1997). The

⁴ http://docs.scipy.org/doc/scipy/reference/generated/scipy.optimize.differential_evolution.html

Table 4. χ^2 estimates of the converged minimization process for five combinations of test distributions.

Test distribution		χ^2
for N_{cells}	for n_{var}	
uniform	uniform	226 ± 4
normal	normal	221 ± 2
log-normal	log-normal	211 ± 1
log-normal	power-law	209 ± 3
normal	power-law	205 ± 1

cell variation rate would be additionally modulated by relativistic time effects and the source redshift. Thus, modelling a direct correspondence between jet properties and the cell variation rate is beyond the scope of this simplistic modelling approach. Therefore, we stick to these four generic distributions.

We test five combinations of distributions for the two model parameters as shown in Table 4. We run the minimization process described in Section 5.1 for each combination of distributions three times to check whether the process converges at the same χ^2 and the same best-fitting parameters. We discuss the results of the minimization process in the following section.

An alternative approach to the minimization process described in Section 5.1 is to keep the two model parameters for each source as variable in a Markov chain Monte Carlo procedure, minimizing the χ^2 -statistic of Eq. (8). This procedure does not require an assumption about the distributions of the number of cells and cell variation rates. But with two parameters for 62 sources this procedure is a minimization over a 124 dimensional parameter space and computationally not feasible.

5.1.2 Results

Table 4 lists the minimized χ^2 , averaged over the three repetitions of the minimization process, and the corresponding standard deviation for the five different combinations of test distributions. The minimized χ^2 ranges between 205 and 226, showing that the best-fitting model does not strongly depend on the choice of the two model distributions. The minimum χ^2 is achieved with a truncated normal distribution $N_{\text{trunc}}M_c, S_c$ for the number of cells and a power-law distribution $\mathcal{P}\mathcal{L}\alpha_v, L_v, U_v$ for the cell variation rate. Therefore we limit all following discussion to this combination of test distributions.

Figure 13 visualizes the progression of the differential evolution algorithm during one minimization process. Every iteration represents one random pick of parameters⁵ $p = M_c, S_c, \alpha_v, L_v, U_v$. Panel (a) shows the progression of $\chi^2 p$ over the iterations. The solid line represents the mean over the previous 100 iterations and the filled area the corresponding standard deviation. χ^2 shows a decreasing trend and the spread is generally decreasing⁶, indicating that the minimization process is converging.

⁵ This set of parameters may or may not be accepted as potential solution by the algorithm.

⁶ Before accepting a solution the algorithm draws random picks throughout the parameter space to test, if it got stuck in a local

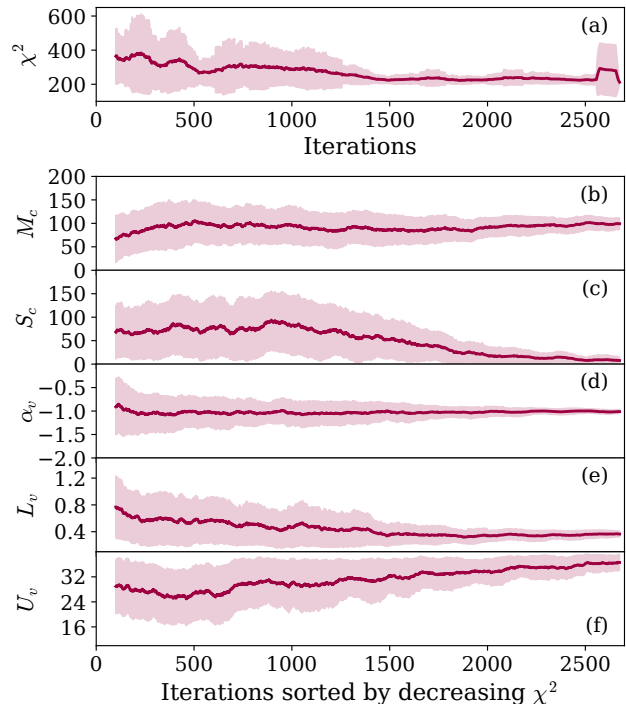


Figure 13. Progression of the χ^2 -minimization (panel a). Each iteration refers to one randomly picked set of parameters $p = M_c, S_c, \alpha_v, L_v, U_v$. These parameters are shown in panels b–f. All parameter values are sorted by decreasing χ^2 . In each panel, solid lines show the mean over the previous 100 iterations, filled regions visualize the corresponding standard deviation.

Panels (b)–(f) show the progression of the five distribution parameters $M_c, S_c, \alpha_v, L_v, U_v$, sorted by decreasing χ^2 . The solid line and the filled area illustrate the average and standard deviation over the previous 100 iterations. All parameters are approaching a constant value and the spread starts to decrease at some point in the minimization progress, indicating good convergence. The spread during the last iterations indicates how well the parameter is constrained. The process shown in Fig. 13 converges at $M_c = 112, S_c = 2, \alpha_v = -1.0, L_v = 0.4, U_v = 38$ with $\chi^2 = 205$. All repeated minimization processes converge at the same values within the uncertainties indicated in Fig. 13.

Under the assumption that all 62 sources of the RoboPol main sample follow the tested random walk process, the result of the minimization shows that all sources have roughly the same number of cells, $N_{\text{cells}} \sim 112 \pm 2$, and the cell variation rates range between ~ 0.4 and 38 cells per day, whereas lower rates are more likely than higher rates. With 63 degrees of freedom $\chi^2 = 204$ refers to a p-value of $\sim 10^{-16}$. Based on this p-value the hypothesis that the observed rotations are produced by the random walk process with objects picked from the parameter space described by $M_c, S_c, \alpha_v, M_v, S_v$ is therefore rejected at high significance. Since several bins contain only a few data points (cf. Fig. 12), this χ^2 -test is not a reliable hypothesis test. Therefore, we

minimum. These tests are indicated by the increased χ^2 during the last ~ 200 iterations.

use the χ^2 -minimization just to constrain the $N_{\text{cells}}, n_{\text{var}}$ parameter space and run additional tests in the following section, based on the optimized parameter space found here.

5.2 Simulated rotation samples

With $M_c, S_c, \alpha_v, L_v, U_v$ fixed by the previous minimization process, we create random samples of rotations following steps (ii) and (iii) in Section 5.1. Then, the rotations are identified in the simulated data set and the distributions of the resulting rotation parameters are compared to the observed ones (cf. Figs. 3 to 6) with a two-sample Kolmogorov-Smirnov (KS) test.

We run 5000 simulations, each producing a data set with the same number of sources and periods per source as well as similar period durations, time sampling, and uncertainties as the RoboPol data. Each coloured line in Fig. 14 is based on one simulation, showing the ECDF of the rotation amplitudes (panel a), durations (panel b), rates (panel c), and variation estimator (panel d). Red lines are based on large rotations, whereas blue lines include all rotations with arbitrary amplitudes. The ECDFs are shown for 100 simulations. Black lines (dashed and solid) show the corresponding observed distributions.

The inset histograms show the distributions of p-values resulting from the two-sample KS-tests comparing each simulated distribution to the corresponding observed distribution of rotation parameters. Blue histograms correspond to the distributions based on all rotations (blue ECDFs and black solid line), red histograms to the distributions based only on the large rotations (red ECDFs and black dashed line). The hypothesis that the compared distributions come from the same parent distribution, i.e., that the observed rotations originate from the tested random walk model, cannot be rejected for any of the rotation parameters at any reasonable significance level ($\alpha \leq 1\%$). When we consider all three independent parameters characterizing the rotations – amplitude, duration, and variation estimator – simultaneously, 74% of the simulations are not rejected in any of the three KS-tests at 1%-significance level, based on all rotations. Considering only large rotations, 77% of the simulations are not rejected.

Whereas the KS-tests do not reject the hypothesis that the entire sample of rotations in the RoboPol main sample is produced by the tested random walk process, a direct comparison of the observed and simulated ECDFs of the rotation parameters in Fig. 14 shows that the distribution of parameters is not exactly reproduced. Comparing first the distributions including all rotations (black solid and blue lines), the distribution of rotation amplitudes (panel a) is reconstructed well by the random walk process. But simulated rotation durations (panel b) are mostly larger and rotation rates (panel c) accordingly slower than the observed ones. 38% of the simulated duration ECDFs lie entirely right of the observed ECDF, and 21% of the rotation rate ECDFs lie entirely left of the observed one⁷. The ECDFs of the variation estimator (panel d) indicate that the simulated rotations are on average less variable than the observed ones.

A comparison between the simulated and observed

ECDFs based on only the large rotations (black dashed and red lines) gives similar results and the observed and simulated ECDFs differ even more. The reason is that the minimization process described in Section 5.1 that tries to find the optimal model parameter space uses all rotations, which are dominated by small rotations (Table 2). Therefore, the minimization process is more likely to match the ECDFs of all rotations than the large rotations. This could indicate that the variability process responsible for the small rotations could be explained more easily with a random walk process, while the large rotations are less likely to follow a random walk process. The amplitude cut between two different processes is not necessarily at a value of 90 degrees, though, or clearly fixed at all. Running this analysis only on a sub-sample of rotations – small and large ones individually – is currently not possible, because the number of rotations is not large enough. Therefore, we restricted this model test to trying to explain the entire sample of rotations with the same process, without applying an arbitrary amplitude cut.

5.3 Polarization fraction of random walks

With $M_c, S_c, \alpha_v, L_v, U_v$ fixed by the minimization process, we create samples of random walk simulations as in the previous section, but here we focus on the polarization fraction. For each simulated object we estimate the mean and standard deviation of the polarization fraction during rotation periods, non-rotation periods and in general.

Figure 15 shows ECDFs of the mean (panel a), the standard deviation (panel b), and the ratio of the two for 100 out of 5000 random samples (blue lines) in comparison to the distributions estimated from RoboPol main sample (black lines). The simulated and observed distributions of the mean and standard deviation of the polarization fraction differ significantly. Two-sample KS-tests give p-values in the range of 10^{-5} – 10^{-1} for the mean polarization fraction, rejecting 85% of the simulations at 1%-significance level, and 10^{-4} – 10^{-1} for the standard deviation of the polarization fraction with a rejection rate of 54%. A direct comparison shows that the range of the simulated mean and standard deviation of the polarization fraction is much narrower than in the observed data. The origin of this narrow distribution is the small range of cell numbers that has been found by the minimization process in Section 5.1, which the simulated sources are drawn from. As shown in Fig. 5 of Kiehlmann et al. (2016) the mean and standard deviation of the polarization fraction correspond to the number of cells in the random walk model and are thus limited by the allowed range of cell numbers.

Despite this result, the ratio of the standard deviation and the mean is comparable to the observations. At 1%-significance level only 2% of the simulations are rejected. The reason is that this ratio typically is close to a value of 0.5 in the random walk simulations as discussed in Kiehlmann et al. (2016), which is what we also observe in the data.

The ratio between the mean polarization fraction during large rotations and during non-rotation periods as well as the corresponding ratio of standard deviations as observed in the data is reproduced by the simulations (Fig. 16, black dashed and red lines), showing that a drop of the mean polarization fraction during large rotations is consistent with a random walk process. This is not the case when considering

⁷ In this analysis we exclude the 20 smallest and 20 largest values.

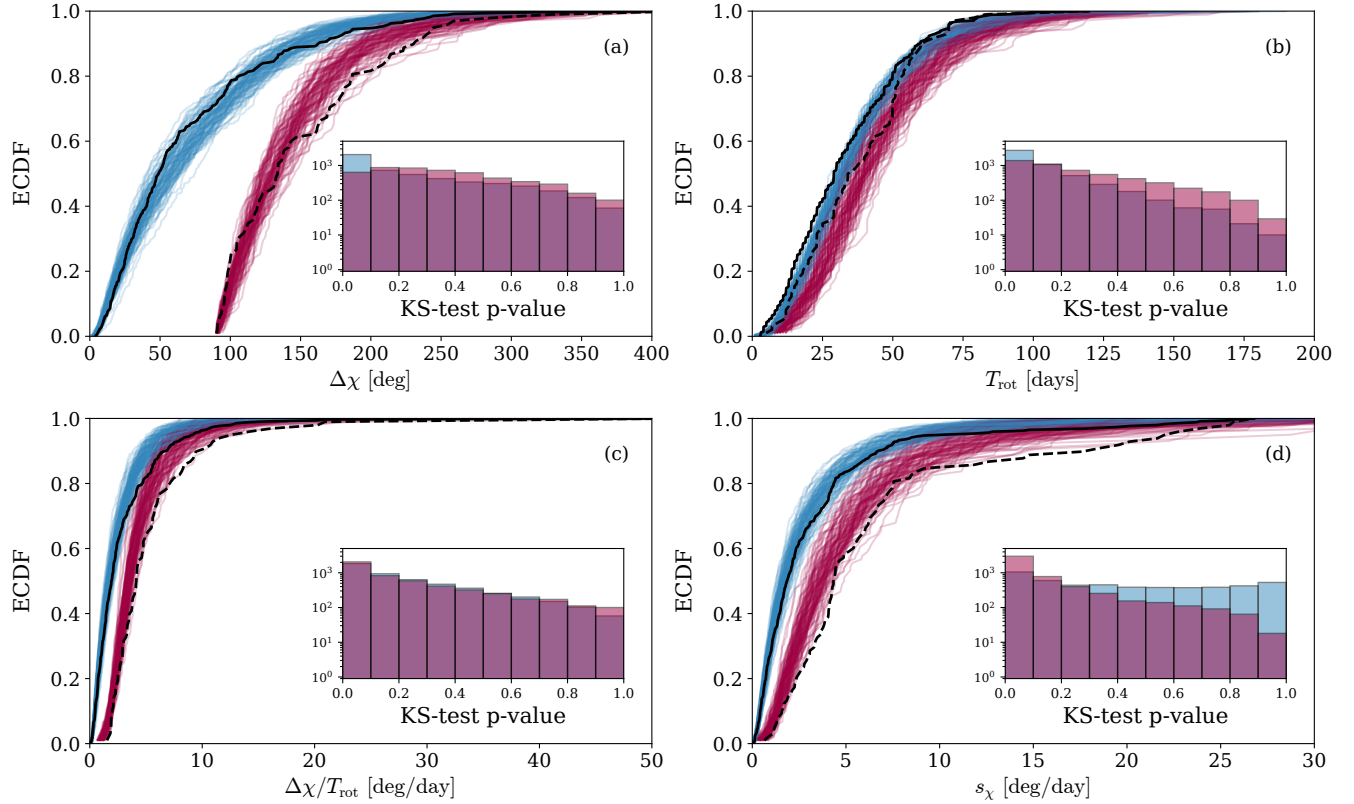


Figure 14. Cumulative distribution functions of rotation amplitudes (*panel a*), durations (*panel b*), rates (*panel c*), and variability (*panel d*). Coloured ECDFs are results of the random walk simulations: blue ones are based on rotations with arbitrary amplitudes, red ones on rotations larger than 90 deg. Each coloured ECDF corresponds to one of 500 simulations. Solid and dotted, black lines are the corresponding distribution functions based on the RoboPol main sample. Inset histograms show the distribution of p-values resulting from the KS-tests comparing the blue simulation ECDFs with the observed, solid black line ECDF.

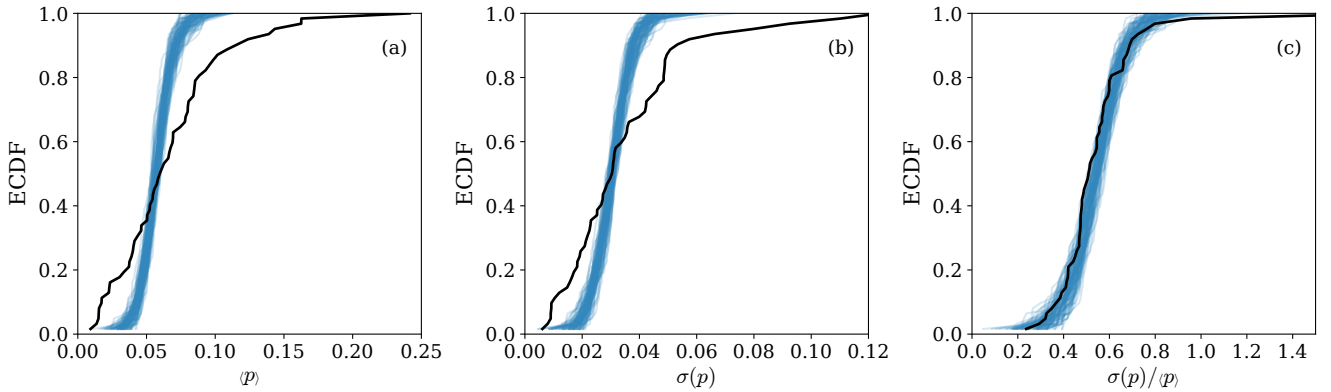


Figure 15. Cumulative distribution functions of the mean (*panel a*) and the standard deviation (*panel b*) of the polarization fraction. Coloured ECDFs are results of the random walk simulations. Black lines are the corresponding distribution functions based on the RoboPol main sample.

rotations with arbitrary amplitudes (black solid and blue lines), where 95% of the simulations are rejected at 1%-significance level based on two-sample KS-tests. The simulated distributions are much narrower than the observed

ones, owing to the narrow distributions in the mean and standard deviation of the polarization fraction (Fig. 15).

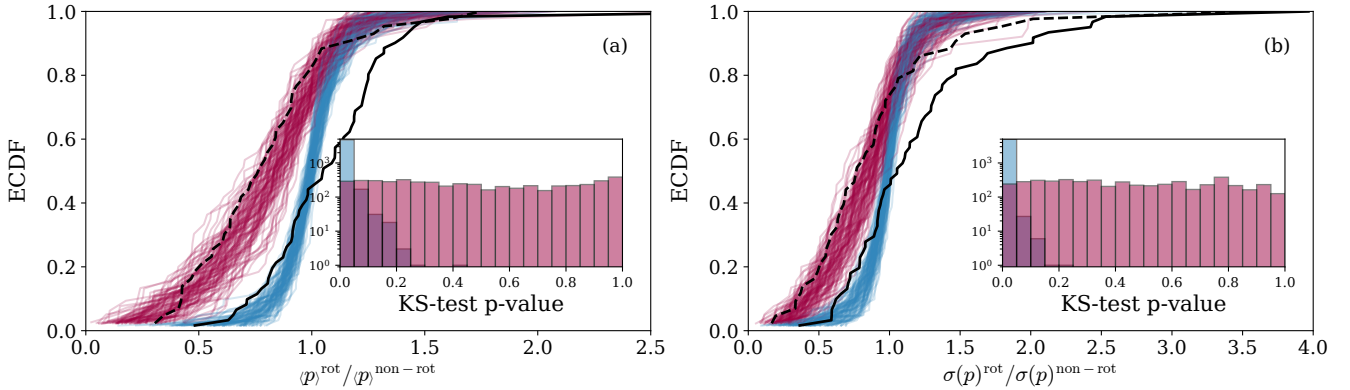


Figure 16. Cumulative distribution functions of the ratio of the mean polarization fraction comparing the rotation periods to the non-rotation periods (*panel a*) and the ratio of the the standard deviation (*panel b*) accordingly. Coloured ECDFs are results of the random walk simulations: blue ones are based on identified rotations with arbitrary amplitudes, red ones on rotations larger than 90 deg. Each coloured ECDF corresponds to one of 500 simulations. Solid and dotted, black lines are the corresponding distribution functions based on the RoboPol main sample. Inset histograms show the distribution of p-values resulting from the KS-tests comparing the blue simulation ECDFs with the observed, solid black line ECDF.

5.4 Likelihood of observing no rotations

Blinov et al. (2016b) argue that there are probably two classes of blazars in the RoboPol main sample: those which exhibit large ($\Delta\chi \geq 90$ deg) EVPA rotations ($\sim 25\%$ of the sources) with an average frequency of one per 230 days, and those which do not or rarely show rotations with a estimated frequency of less than one per 2900 days. We note that in this study, as we use a less conservative method to identify rotations, 43 out of 62 sources (69%) show at least one large rotation. We estimate the probability of observing N_{rot} rotations within time T under the hypothesis that the polarization variability is produced by the tested random walk process, using the Poisson distribution

$$PN_{\text{rot}}, \lambda, T = \frac{\lambda T^{N_{\text{rot}}}}{N_{\text{rot}}!} e^{-\lambda T}, \quad (9)$$

where λ is the average frequency of rotations. We use the frequency of rotations with amplitudes $\Delta\chi \geq 90$ deg as shown in the mid panel of Fig. 10 as estimates of λ , depending on the model parameters N_{cells} and n_{var} . Figure 17 shows the probability of observing zero, one, or two rotations in the median RoboPol period, $T_{\text{obs}} = 135$ days, over a range of model parameters. Observing one large rotation is generally more likely than observing no large rotation throughout the tested parameter space. In the optimal parameter space the probability of observing no large rotation within a period of $T_{\text{obs}} = 135$ days ranges between 23% and 60%, consistent with the 33% of RoboPol sources not showing large rotations. We note, though, that we do not account for multiple observing seasons in this comparison. This is considered in the following test.

As in the previous sections, we construct simulated source samples. Here, we count the number of sources showing $N_{\text{rot}} = 0, 1, 2, \dots$ rotations with large amplitudes, $\Delta\chi \geq 90$ deg. Based on 5000 simulations, Fig. 18 shows distributions of the number of sources with N_{rot} rotations. The number of sources showing N_{rot} in the RoboPol sample are marked by vertical lines and are consistent with the simu-

lated distribution. Thus, the random walk model produces similar numbers of rotations per sources as observed in the data and is *consistent with a fraction of sources exhibiting no rotations within the typical observing periods of the RoboPol program.*

6 DISCUSSION

Aiming at explaining the polarization variability of a sample of blazars we have used a simplistic two-parameter random walk model. In this framework we assumed that the sources are located in a limited range of the model parameter space and we have constrained this range through an optimization process that tries to reproduce a sample of EVPA rotations detected in the RoboPol main sample, with rotation parameters similar to the observations. We simulated an entire sample of sources, randomly located in this optimized parameter space, and tested these simulations against the data.

We have found that our model produces a number of large EVPA rotations ($\Delta\chi \leq 90$ deg) comparable to the observations. The fraction of sources not showing rotations is reproduced by the model as a result of the limited duration and number of periods and a range of variability time-scales (0.4–38 cells changing per day in the observer frame). This implies that *in the framework of a random walk process we would expect to see rotations in all sources, when the observations are long enough.* Only long-term monitoring could help to further constrain how rarely some sources exhibit rotations.

The rotations identified in the RoboPol sample were characterized by four parameters – amplitude, duration, rate, and the variation estimator as a measure of smoothness. The distributions of these parameters produced by the model are not rejected in more than 74% of the simulations when compared to the observations using a two-sample KS-test, implying that the model is capable of producing a sample of rotations comparable to that from the RoboPol

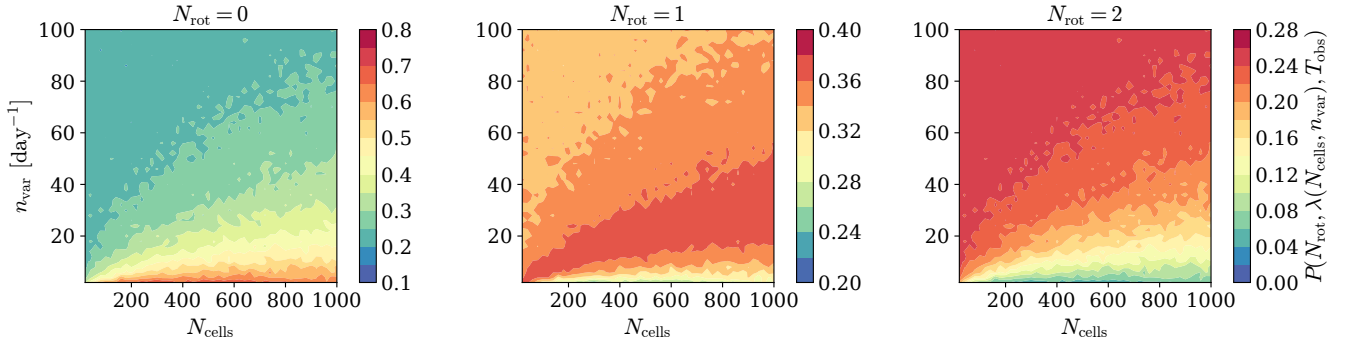


Figure 17. Probability of observing zero (*left panel*), one (*mid panel*), or two (*right panel*) rotations within the median period of the RoboPol sample, $T_{\text{obs}} = 135$ days, from the tested random walk process.

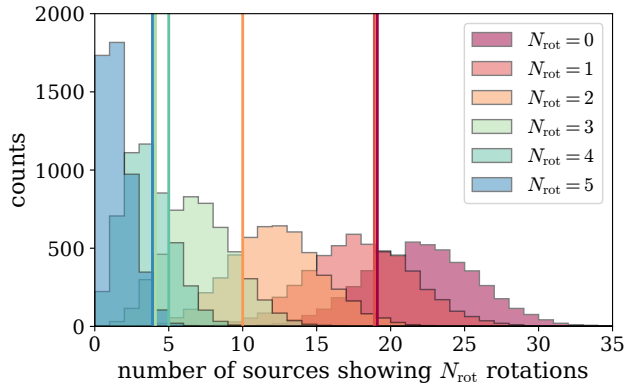


Figure 18. Distribution of the number of sources showing N_{rot} large rotations based on 5000 simulation samples. The number of sources showing N_{rot} large rotations in the RoboPol sample are marked by vertical lines in corresponding colours.

data. Despite the non-rejecting KS-tests the distributions of some rotation parameters are systematically set off from the data. This offset is more pronounced when comparing just large rotations rather than rotations with arbitrary amplitudes. Since the sample of all rotations, which is dominated by small rotations ($\Delta\chi < 90$ deg), is described better by the model than the large rotations, this could imply different processes for the smaller variability and the periods of larger rotations. This has been suggested before, e.g. in Blinov et al. (2015) and Kiehlmann et al. (2016). Furthermore, it would be consistent with the results presented in Blinov et al. (2017, submitted) showing that all large EVPA rotations are potentially occurring contemporaneously with gamma-ray flares. Large rotations may be produced by one process also responsible for gamma-ray flares, whereas small rotations may be a signature of an underlying stochastic process. The superposition of different processes has also been discussed in Angelakis et al. (2016). We point out, though, that two processes would not necessarily correspond to a strict cut in the rotation amplitude.

The model fails to reproduce distributions of the mean and standard deviation of the polarization fraction observed in the RoboPol main sample. The reason is that the model parameter space that is most likely to reproduce the sam-

ple of rotation characteristics is too narrow in the number of cells. This constrains the mean polarization fraction and its standard deviation. While we have shown that there is no need to assume two populations of sources in order to create the apparent dichotomy of rotators and non-rotators reported in Blinov et al. (2016b), two populations centred at different locations in the parameter space could broaden the distributions of the polarization fraction mean and standard deviation and remove the systematic offsets of the simulated rotation parameter ECDFs from the observed ones.

The fact that the entire polarization variability of the RoboPol sample cannot be consistently explained by our modelling approach implies that (a) the simplistic random walk model cannot produce this variability in general, (b) it cannot reproduce the variability for all sources, or (c) we have not correctly constrained the model parameter space from which we randomly draw the simulated source sample. Therefore, we can certainly not accept the model with the discussed constraints on the model parameter space. Neither can we make a strong claim that this random walk model is rejected as an explanation for the variability that we observe in the optical polarization. The fact that this simplistic model and the generic constraints on the parameter space can produce several characteristics we have observed implies that the hypothesis of a random walk model cannot easily be dismissed and should be tested thoroughly.

Complementary to this statistical study that focused on the question whether the optical polarization variability of the entire RoboPol sample can be explained with a simple random walk process, we suggest testing the random walk hypothesis against each source and rotation event individually. Following for example the procedure of Kiehlmann et al. (2016) would constrain the model parameter space for each source individually without requiring an a priori assumption about the distribution of the number of cells and the cell variation rate. Additionally, this approach would allow us to discern whether only particular sources or particular rotation events are consistent with the random walk model. Though much more challenging due to the significantly large model parameter space, more physical models, as presented by Marscher (2014), need to be tested against the data. A particular advantage of more sophisticated models is the multi-frequency coverage. Multi-frequency polar-

ization monitoring could put much stronger constraints on such models.

Our simplistic single-frequency modelling approach demonstrates that the random walk hypothesis should not be dismissed. We have pointed out several features in the polarization variability that are consistent with the tested random walk process:

- Rotations produced by the random walk process have the same dependencies between the characterizing parameters – amplitude, duration, rate, and variation estimator – as observed in the data.
- During rotation periods the polarization fraction on average decreases. In the context of the random walk model rotation periods are not behaving intrinsically differently from other periods. By selecting out periods that show an apparent rotation, we select out periods of lower polarization, which are more likely to show apparent rotations.
- In the data the amount by which the polarization fraction drops during a rotation correlates with the rotation rate. Though not highly likely, it is possible to reproduce this result with the random walk model.

7 CONCLUSIONS

We have searched for rotations of the polarization angle in blazars of the RoboPol main sample using three seasons of data. We have estimated four characteristic parameters for each rotation as well as the polarization fraction during rotations and showed certain dependencies between those parameters. In a statistical approach, we tested whether a simple random walk model can reproduce the entire sample of rotations and their characteristics. The model fails to reproduce the rotation characteristics and the polarization fraction at the same time. But we cannot with certainty state that we have correctly constrained the model parameter space. Therefore, we cannot claim that the random walk model can be rejected.

On the other hand the model succeeds in producing samples of rotations with characteristic parameters similar to the observed ones. Furthermore, it is consistent with the apparent dichotomy of rotators and non-rotators, the drop of the polarization fraction during rotations, and the apparent dependency of the rotation rate on the polarization fraction decrease during rotations. We have pointed out that testing the model against the data for each source or each rotation event individually could help to better understand the limitations of this random walk model and would allow us to test whether only particular sources or types of rotation events are consistent with a random walk. This approach would be complementary to this study that tested whether the polarization variability of the entire RoboPol sample could be explained by a simple random walk model.

The fact that even a very simplified model can reproduce various features that we observe in the data suggests that the random walk hypothesis should be studied in further detail and, in particular, that more physical models should be tested on a statistical basis against large data sets such as the RoboPol main sample of blazars.

ACKNOWLEDGEMENTS

The RoboPol project is a collaboration between the University of Crete/FORTH in Greece, Caltech in the USA, MPIfR in Germany, IUCAA in India and Toruń Centre for Astronomy in Poland. This research was supported in part by NASA grants NNX11A043G and NNX16AR41G and NSF grant AST-1109911. S.K. is supported through NASA grant NNX13AQ89G. This research was partly funded by the Academy of Finland project 284495. S.K. particularly thanks T. Savolainen for comments on this manuscript and for the support of this research. The authors furthermore thank E. Angelakis, T. Hovatta, V. Pavlidou, and K. Tassis from the RoboPol collaboration for comments and intense discussions during the collaboration meetings. This research was done with `python` packages `numpy 1.11.3`, `scipy 0.18.1`, `statsmodels 0.6.1`, `pytables 3.3.0`, and `matplotlib 2.0.0`.

REFERENCES

- Aleksić J., et al., 2014a, *A&A*, 567, A41
 Aleksić J., et al., 2014b, *A&A*, 569, A46
 Angelakis E., et al., 2016, *MNRAS*, 463, 3365
 Blinov D., et al., 2015, *MNRAS*, 453, 1669
 Blinov D., et al., 2016a, *MNRAS*, 457, 2252
 Blinov D., et al., 2016b, *MNRAS*, 462, 1775
 Feigelson E. D., Babu G. J., 2012, *Modern Statistical Methods for Astronomy: With R Applications*, 1 edn. Cambridge University Press
 Holmes P. A., et al., 1984, *MNRAS*, 211, 497
 Jones T. W., Rudnick L., Aller H. D., Aller M. F., Hodge P. E., Fiedler R. L., 1985, *ApJ*, 290, 627
 Kiehlmann S., et al., 2016, *A&A*, 590, A10
 Kikuchi S., Mikami Y., Inoue M., Tabara H., Kato T., 1988, *A&A*, 190, L8
 King O. G., et al., 2014, *MNRAS*, 442, 1706
 Kinman T. D., 1967, *ApJ*, 148, L53
 Konigl A., Choudhuri A. R., 1985, *ApJ*, 289, 188
 Larionov V. M., et al., 2008, *A&A*, 492, 389
 Larionov V. M., et al., 2013, *ApJ*, 768, 40
 Lister M. L., Marscher A. P., 1997, *ApJ*, 476, 572
 Longair M. S., 2011, *High Energy Astrophysics*, 3 edn. Cambridge University Press, <http://amazon.com/o/ASIN/0521756189/>
 Marscher A. P., 2014, *ApJ*, 780, 87
 Marscher A. P., et al., 2008, *Nature*, 452, 966
 Marscher A. P., et al., 2010, *ApJ*, 710, L126
 Nalewajko K., 2010, *International Journal of Modern Physics D*, 19, 701
 Nalewajko K., Begelman M. C., 2012, *MNRAS*, 427, 2480
 Nolan P. L., et al., 2012, *ApJS*, 199, 31
 Pavlidou V., et al., 2014, *MNRAS*, 442, 1693
 Storn R., Price K., 1997, *Journal of Global Optimization*, 11, 341
 Vlahakis N., Königl A., 2004, *ApJ*, 605, 656
 Zhang H., Chen X., Böttcher M., 2014, *ApJ*, 789, 66
 Zhang H., Chen X., Böttcher M., Guo F., Li H., 2015, *ApJ*, 804, 58

This paper has been typeset from a $\text{\TeX}/\text{\LaTeX}$ file prepared by the author.